Results in Engineering 15 (2022) 100531

Contents lists available at ScienceDirect

Results in Engineering

journal homepage: www.sciencedirect.com/journal/results-in-engineering

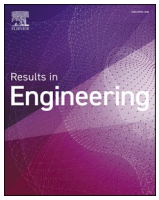

The effective thermal conductivity of virtual macroporous structures

A.J. Otaru [a,*], R.O. Isa [a], A.U. Emene [a], A.A. Faruq [a], P.O. Sedemogun [a], S.M. Hassan [b]

[a] Department of Chemical Engineering, Federal University of Technology, P.M.B. 065, Gidan-Kwanu Campus, Minna, Nigeria
[b] Department of Biochemistry, Ahmadu Bello University, Samaru Campus, 810211, Zaria, Nigeria

ARTICLE INFO

Keywords:
Macroporous structures
Effective thermal conductivity
Modelling and simulation

ABSTRACT

Recent developments in macroporous structures featuring metallic bodies are becoming a focus of research due to their improved load-bearing capacity and high specific surface area, making them potential candidates for thermofluidic applications. Through numerical modelling and simulations at the pore-scale, this paper examines the ability of virtual macroporous structures generated by sphere-packing models to predict the effective thermal conductivity of "bottleneck-type" macroporous structures. Simulations of virtual macroporous structures with monosized pores show the relative impact of key pore structure-related properties on effective thermal conductivity in such structures. The extension of these findings to bimodal and adapted designs results in an increase in fluid transverse capacity of these structures, causing an increase in the original monomodal pore volume by 17 and 30% respectively, while varying their capillary radius from 10 to 80 μm only results in a 10% increase in pore volume fraction. Overall, this study demonstrated that pore structure-related properties played an important role in conductive heat transfer, with material porosity being an influential property and inversely (non-linear) correlated with the effective thermal conductivity of the foam–fluid system. The contributions tendered by material pores and specific surfaces were minimal, and mathematical relationships were proposed between effective thermal conductivity, pore-structure-related properties, and fluid and solid thermal conductivity values. Modelling techniques such as this one could serve to optimize the thermal performance of macroporous structures, as well as to gain the benefits of being ultra-lightweight and having a high Young modulus.

1. Introduction

Scientists and materials manufacturers have devoted decades to the development of cellular metallic components that attempt to replicate substances like wool, kevlar, hemp, melamine, cork, coral, polyurethane, pumice stone, and natural sponge. A rise in the production of cellular metallic components has resulted from increased demand for these materials along with a vested interest in the 2030 United Nations Sustainable Development Goals (SDGs) - a scientific revolution enabled by investments in innovation, industry, and infrastructure. Cellular metals are classified as open-celled or closed-celled depending on their metal cells with air-dominated pores and openings [1,2]. The interconnecting pores in cellular materials allow fluid to penetrate while the skeletal matrices conduct heat and are suitable as load-bearing materials. Prevalent opinions in the literature [3,4] classify open-celled foams as porous metals while close-celled foams are regarded as metal foams. The predominant characteristic of these structures' porosity, typically 80–95% [3], causes them to be classed as porous metals, 50–75% as metal foams [5], and 70–80% as semi-open-celled metallic foams [3], wherein generally, they are referred to as cellular metals [6,7].

The size and shape of cellular materials are influenced by the manufacturing technique and operating conditions used. Fig. 1 illustrates cellular metallic structures produced by replication casting, showing typical near-spherical pore openings, as well as monomodal [8] and biomodal [9] pores embedded in porous matrix interstices. Several of these materials' notable features, including their high surface area, high Young modulus, incredibly low weight (yet very robust), and high porosity, make them effective for a broad range of multifunctional applications. These include heat dissipation media (heat exchangers and heat pipes), the automotive and aerospace industries, petroleum reservoirs, fluid distribution in fuel cells, solar collectors, filters, catalyst carriers, sandwich structures, electrolytic operations, biomedical implants, batteries, self-lubricated bearings, soundproofing, and vibration control devices [1,10,11]. As catalyst carriers in chemical and combustion processes, their irregular structure and high porosity ensure intensive gas reactions [12]. Comparatively to fibrous materials and dense polymers, cellular metals exhibit higher mechanical strength and higher impact-energy absorption capacities while retaining their

* Corresponding author.
E-mail address: otaru_12257@yahoo.com (A.J. Otaru).

https://doi.org/10.1016/j.rineng.2022.100531
Received 6 June 2022; Received in revised form 26 June 2022; Accepted 4 July 2022

Nomenclature

List of symbols

2D	Two-dimensional
3D	Three-dimensional
DEM	Discrete element modelling and simulation
D_p	Pore-diameter [mm]
D_w	Pore-diameter openings [mm]
ϵ	Foam porosity [%]
eff	effective
f	Fluid
FE	Finite element
K	Thermal conductivity [$W.m^{-1}.K^{-1}$]
L – L	Large – Large
L – S	Large – Small
LVT	Laguerre – Voronoi Tessellations
MCells	Million cells
$MgCl_2$	Magnesium chloride
NaCl	Sodium chloride
RVE	Representative volume element
r_c	Capillary radius [μm]
r_p	Pore – radii [mm]
r_w	Pore opening radius [mm]
s	Solid
θ	Wetting angle [degree]
σ_{xy}	Surface tension [$N.m^{-1}$]
μCT	Micro computerised tomography

topology at higher temperatures and pressures. These structures are subject to complex phenomena of thermal exchange between cell walls or skeletal matrix and pore fluid based on the properties of the base material (aluminum, copper, nickel, titanium, zinc, steel, silver, iron and alloys), pore structure properties (porosity, surface area, tortuosity, pore openings and cell size) and fluid properties (air, water, carbon dioxide, methane, ethylene glycol) [13]. For this reason, an accurate understanding of how changes in foam-fluid properties affect the effective thermal conductivity is critical in order to enhance the efficiency of the heat transfer rate, resulting in energy savings and more compact and lightweight structures.

The use of conduction in solid body systems is widely recognized as the principal mode of heat transfer [14,15], and its applications to the understanding of heat transport phenomena and effective thermal conductivity in metal foam-fluid systems have been extensively studied. Research in this field has employed experimental, asymptotic, empirical, analytical and numerical techniques to estimate the effective thermal conductivity (K_{eff}) of foam-fluid systems. Calmidi & Mahajan (1999) [15] used an experimental approach to predict the effective thermal conductivity of high porosity ($0.90 \leq \varepsilon \leq 0.98$) aluminium foams saturated with air and water. In spite of a linear inverse relationship between foam porosity (ε) and K_{eff}, their findings did not reveal a systematic effect of cell size on the effective thermal conductivity of the foam-fluid system. Their work also investigated the role of heat dissipation induced by hydrodynamic phenomena for foam-water systems; it was considered almost negligible for air-filled foams because the skeletal phase is relatively conductive. Experimental measurements K_{eff} of porous Aluminium foams in Ref. [16] confirm the linear inverse relationship

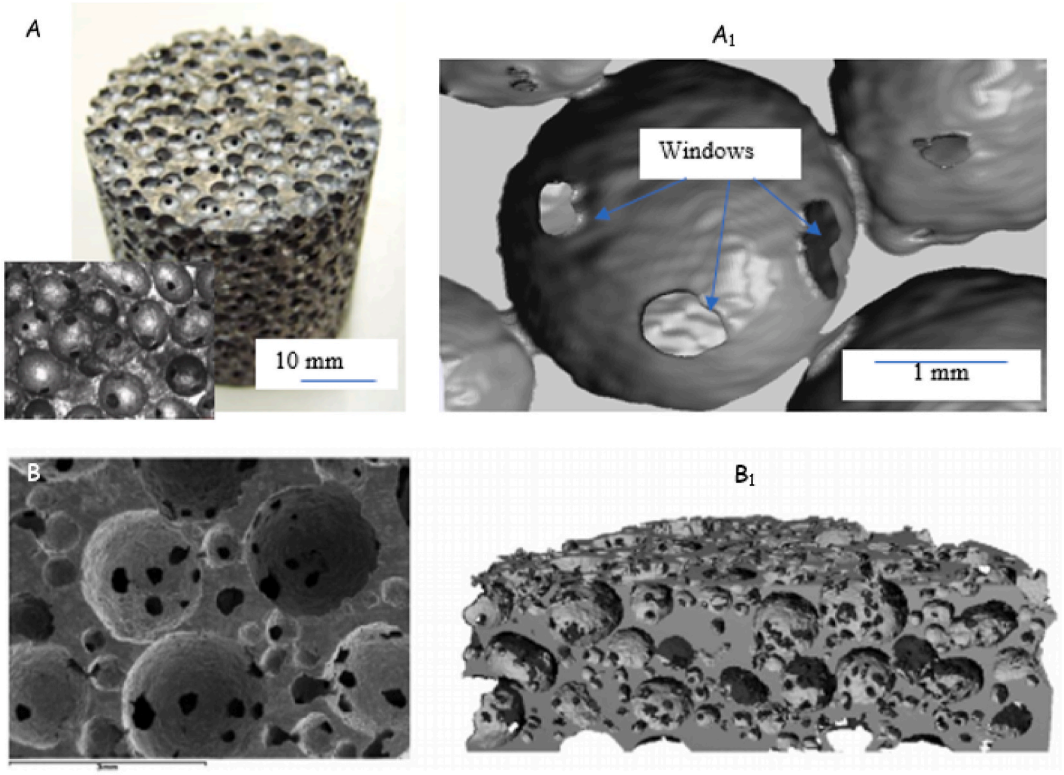

Fig. 1. Top left: An optical micrograph of a porous sample made from near-spherical mono-sized NaCl cast in vacuum [A]. Top right: An X-Ray computerised tomography (μCT) image of typical monomodal pores (adapted from Ref. [8]) [A_1]. Bottom left [B] and bottom-right [B_1] are scanning electron microscopy (SEM) images for bimodal "bottleneck-type" structures made by adding 25 vol% small-sized [0.5–1.0 mm] into large-sized [2.0–2.5 mm] packed NaCl (adapted from Ref. [9]).

between porosity and effective thermal conductivity of high porosity foams discussed in Ref. [15], despite changes in the properties of fluids and base metals. In this study, the solid-lattice orientations in metal foams were shown to have a relative effect on heat transfers over the gaseous phase; however, the individual impact of the pore-structure-related properties of the porous medium was not captured. Paek et al., 2000 [17] also found a linear inverse relationship between K_{eff} and foam porosity (ϵ) after conducting a series of experiments on one-dimension conduction heat transfer across the interstices of porous aluminium foams. There were no noticeable changes in K_{eff} resulting from variations in the cell size of the porous structures with a fixed porosity. Informed by the work in Ref. [15], Boomsma and Poulikakos [18], proposed a three-dimensional (3D) structure-based model to account for the K_{eff} of high porosity foams by assuming a representative unit cell metal foam as a Kelvin "tetrakaidecahedron" with cylindrical ligaments and nodes. Their work provided insight into the reliability of using a 3D unit cell approach in obtaining K_{eff} values of porous metals, but an inaccuracy was found [19] in their model and a corrigendum was provided [20] to support their earlier published article [18]. Ranut et al. [11] demonstrated that pore-level numerical methods working from high-resolution tomography datasets could be used to determine the K_{eff} for high porosity foams with reasonable values when compared to experiments. Simulations revealed the dependence of K_{eff} on the conductivity of the solid ligaments with a small contribution from the fluid phase. Based on a similar computational approach in Ref. [11], Fan et al. [21] found that the local anisotropic characteristics of a $\beta-SiC$ foam have an impact on simulated K_{eff} values ranging between 4 and 23%. As well, this study found that saturating porous foams with air had a lower effective thermal conductivity than saturating the pore region of these materials with water. The local anisotropic feature (difference in strut paths) within the computational domain was also observed to contribute to the heat transport mechanisms of these porous materials.

The majority of research works on conductive heat transfer in cellular metallic foams focus primarily on high porosity metallic structures [11–14,22–26] while few works are available on low porosity foams. As an example, experimental measurements by Dukhan and Chen [27]confirm the inverse relationship between porosity and thermal conductivity for low-porosity foams with no noticeable differences for differing cell sizes. Experimental techniques using a transient plane source were applied in Ref. [28] to calculate the K_{eff} of AlSi7 foams with low porosity ($0.5 \leq \varepsilon \leq 0.8$). Their experimental data showed an inverse quadratic dependence of K_{eff} on foam porosity and a significant dependence within the measurement range in which experiments were conducted. Abuserwal et al. [29] used a steady-state experimental technique to account for the K_{eff} of air-saturated low-porosity ($0.5 \leq \varepsilon \leq 0.8$) aluminium foams manufactured with the replication casting technique. The experimentally measured data were found to be consistent and in line with those reported in Ref. [28] with some deviation attributed to the thickness and morphology of the materials within the porous structures. An analysis of the influence of pore size and porosity ($0.73 \leq \varepsilon \leq 0.97$) variation on the K_{eff} of low to high porosity cellular metals was conducted using a Laguerre-Voronoi Tessellations (LVT) simulation in Ref. [30]. The numerical simulations indicated a strong dependence of thermal conductivity on porosity, while there was little or no change observed with variable cell sizes in agreement with experimental descriptions in Refs. [28,29]. In contrast to analogous research done on conductive heat transport in low and high porosity foams, there is little evidence that pore openings and pore size have a discernible effect on the effective thermal conductivity of metal foams. Therefore, this paper examines the effect of pore-structure-related properties on the K_{eff} of virtual macroporous structures derived from a sphere-packing model. The present study differs from previous publications by demonstrating how pore structure-related properties (such as pore openings, pore size, specific surfaces, and capillary radius) affect K_{eff} of virtual microcellular structures. More importantly, this study uncovers the impact of a bimodal arrangement and the adaptation of macroporous structures, as well as K_{eff} dependency on pore structure-related properties of these structures.

2. Research approach

To determine the effective thermal conductivity of fluid saturated virtual macroporous structures ("bottleneck-structures" in this study), a pore-level predictive approach is employed. This approach involves the creation of three-dimensional representative volume elements (3D RVE), followed by a numerical modelling and simulation of conductive heat transfer. In a previous study in Ref. [31], discrete element modelling (DEM) and simulation packing of spherical structures were used to visualize macroporous structures resembling porous metals made by replicating salt beads under low pressure or by casting (Fig. 1). Otaru and Kennedy [32] investigated Darcian permeability for these structures by numerically resolving the pressure drop performance against creeping flow rates for representative volume elements with monomodal pores (1–3 mm) and packing conditions ranging from loose (0.57 to dense (0.67) packing fractions. This study utilizes the approach presented in Ref. [32] and an advanced imaging technique to create three-dimensional representations of foam-fluid systems. MatlabTM code was used to create two-dimensional (2D) slices of binary structures composed of x, y, and z particles (25 μm voxel size) connected by spheres whose capillary radius varied between 10 and 80 μm. For replication casting, the size of the pore diameter openings (r_w) is described in Ref. [33] as a function of the differential pressure (P_i) employed to drive liquid melts into convergent gaps created by packed beds of porogens (e.g. sodium chloride [NaCl] salts or magnesium chloride [MgCl2]). This is related to the capillary radius (r_c), pore opening radius (r_w), wetting angle (θ), surface tension (σ_{xy}) and pore radii (r_p) in virtual packing using the Young-Laplace equation provided below and are geometrically represented by Fig. 2.

$$r_w = \frac{2\sigma_{xy}}{P_i} cos\theta \quad (1)$$

$$r_w = \sqrt{(r_c + r_p)^2 - r_p^2} - r_c \quad (2)$$

The Young-Laplace equation (Eqn (1)) describes the analogy between the capillary radius (in a virtual sense) and the differential pressure applied to permeate liquid metal into convergent gaps created by packed porogen during the packed bead replication casting process. At very high applied differential pressures, the liquid melt dynamically permeates into narrow regions created by the packed beds (a negative of replicated foam) and reduces the size of the openings "windows", creating a foam structure with lower porosity and an increased specific surface area [28,33]. The opposite occurs when differential pressures are low, resulting in higher porosity foams with a smaller surface area and wider openings [31]. According to the experiment described in Ref. [1], liquid metals can be infused into densely and loosely packed beds in order to produce higher and lower porosity foams.

A 3D image processing and model generation software (ScanIP module from Synopsys-Simpleware™) was then used to process the two-dimensional (2D) DEM slices (obtained as TIFF files from Matlab™). Before rendering the binary images into a 3D volume, the 2D binary images were thresholded to capture the pores and openings. By shrinking a larger volume into a smaller unit cell until the volume fractions of the control volume converge to ±2% of the bulk value, a representative volume element (RVE) was determined to be three times the mean pore size. Optimizing the smoothing process in the software's ScanIP module provided accurate representations of pores, openings, volume and shape. This was achieved by using the inbuilt smart mask filter with an optimized iteration number of 10 that preserved the geometrical features of the RVE structures. The 3D RVE porous matrices were directly measured for pore openings, surface area, specific surface (surface area divided by bulk volume), volume and total porosity. The

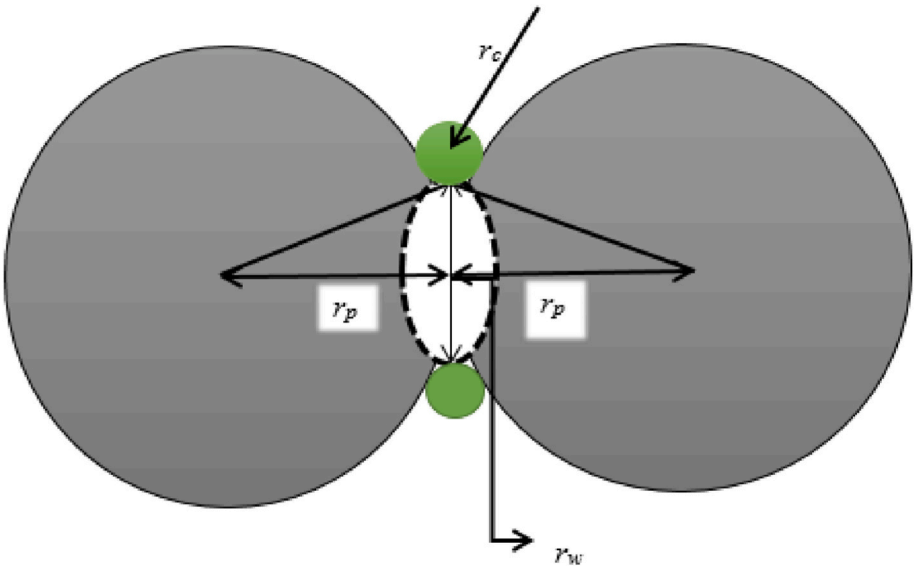

Fig. 2. An illustration of the geometry and notation of connecting spheres.

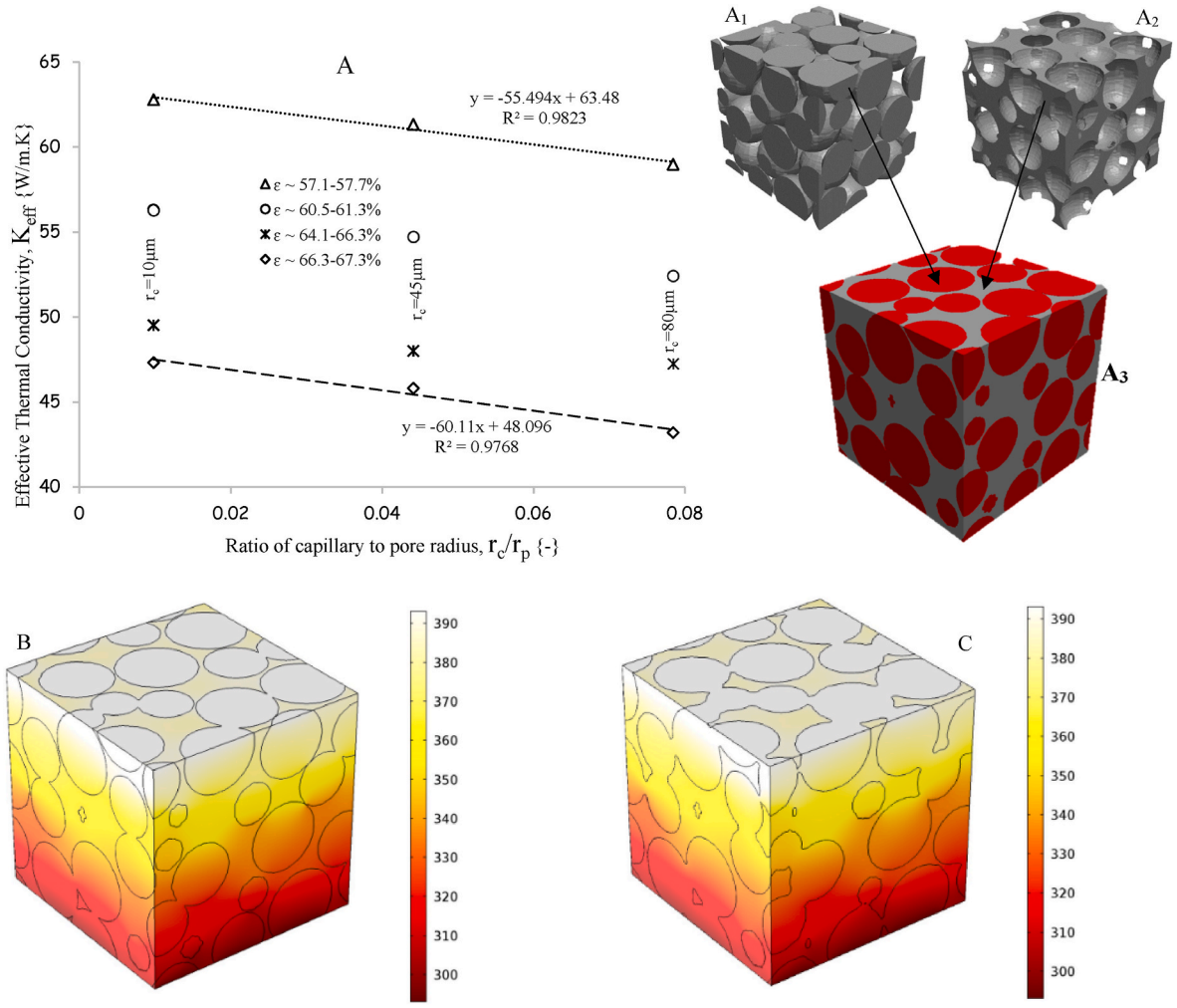

Fig. 3. The three-dimensional (3D) representative volume element showing typical fluid phase [A_1], structural/foam phase [A_2], and foam-fluid system [A_3] appears on the right of the plots of the effective thermal conductivity K_{eff} {$W.m^{-1}.K^{-1}$} against a dimensionless ratio of normalised capillary radius [A]. Fig. 3B and C illustrate the geometrical features and thermal profile profiles {°C} generated with a capillary radius of 10 and 80 μm respectively.

mean pore sizes were measured by watershed segmentation (disconnecting particles) of the RVE spheres and taking an average value of their diameter. Boolean inversion of a 3D RVE structure was used to construct the fluid phase, and superimposition of the two domains was used to construct the foam-fluid system.

The temperature distribution across RVE structures was represented using a fully convergent mesh structure and counting method (developed in Synopsys-Simpleware™ + FE) that provided fast convergence at minimal computational cost and error. A linear tetrahedral mesh structure with a constant growth rate of 1.3 was applied to the discretization of the foam-fluid systems yielding a cell count ranging between 2.5 and 3.5MCells while maintaining a minimum and maximum edge length of 2.0x and 7.0x image resolution, respectively. COMSOL Multiphysics software was used to numerically simulate one-dimensional steady-state conduction across the meshed representative foam-fluid structures by importing them into the heat transfer module. Both the fluid and solid domains were considered to have the same physics of conduction because the interstitial fluid was assumed to be motionless [11,18,34] while maintaining a difference in temperature of 100 °C between the inlet and outlet fluid. The lateral faces and walls were assumed as thermally insulated surfaces. Water (0.6 W m^{-1} K^{-1}) and air (0.024 W m^{-1} K^{-1}) were each considered as the interstitial fluid, while pure aluminium (238W.m^{-1}. K^{-1}), aluminium alloy Al3003–H18 (155 W m^{-1} K^{-1}), alumina (27 W m^{-1} K^{-1}) and concrete (1.8 W m^{-1} K^{-1}) served as base solids. The effective thermal conductivities (K_{eff}) of the RVE foam-fluid systems were evaluated by multiplying the ratio of computed heat flux (q, [W.m^{-2}]) to the temperature gradient (T_{zz}, [K. m^{-1}]) by a negative sign. The selection of boundary conditions, physics, and other methods used to calculate effective thermal conductivities of these materials are similar to those found in Refs. [15,35–37].

3. Discussion of results

Fig. 3 shows the resulting three-dimensional (3D) images and preliminary simulations, which were conducted on several 3D foam-fluid systems with a constant mean pore size of 2 mm in order to determine effective thermal conductivity at the limits of capillary radius. Figures A_1, A_2 and A_3 respectively show 3D representations of a typical fluid, foam (solid) and foam-fluid system for these structures. Fig. 3A plots computed values of K_{eff} against the normalised capillary radius (r_c/r_p), showing that there is an order of magnitude difference between structures with high and low capillary radius, as well as variable porosity measurements. Based on the response to changes in capillary radius, three groups can be distinguished: the most extreme value of K_{eff} was observed for the structure with the highest capillary radius ($r_c \sim 80\ \mu m$), and similar intermediate trends were observed in structures created at intermediate capillary radius ($r_c \sim 45\ \mu m$), where the highest value of K_{eff} was observed for the structure with the lowest capillary radius ($r_c \sim 10\ \mu m$). The effective thermal conductivity was observed to be higher in structures with lower porosities in comparison with those with higher porosities. Further, the linear inverse fall in K_{eff} with increasing capillary radius could also be attributed to slight changes in other pore-structure properties, such as specific surface and material porosity. Fig. 3B illustrates the morphology and thermal distribution for the virtual macroporous foam-fluid structure created at a capillary radius of 10 μm, a pore size of 2 mm, and a mean pore opening of 274 μm, which is less than twice that of the structure (Fig. 3C) created at an 80 μm capillary radius. The heat transfer from regions of higher temperatures to regions of lower temperatures is illustrated in the legend of these foam-fluid systems from entry to exit. Using this analogy, it is presumed that heat transfer occurs primarily in solid structures rather than fluids in the interstices of foam matrices, which is in agreement with experiments on the thermal conductivity of realistic porous metals conducted by Calmidi & Mahajan [15]. Thus, an increment in the capillary radius (reduced infiltration pressure) increases pore openings and leads to a reduction in the volume of the solid structure and, consequently, a lower effective thermal conductivity. As the capillary radius decreases, the solid surfaces/content with the metal matrix becomes larger, and the pore volume reduces, resulting in greater K_{eff}. This means that the relationship between the effective thermal conductivity of these foam-fluid systems and the capillary radius can be described by a linear inverse, as shown in Fig. 3A.

The influence of material porosity and the specific surface is further explored by creating facsimiles of the original virtual macroporous structures but for much lower and higher porosities while maintaining a similar pore distribution. The erosion of the original structures was achieved by removing or adding a number of pixels (typically one to five) to the 3D RVE structural phase, which was then inverted to create the fluid domain. Both domains were then superimposed to create a new foam-fluid system. The erosion was performed in accordance with a study previously reported in Ref. [33] but was extended to include dilation effects in the present work, which resulted in a more comprehensive change to the matrix properties. Material porosity changed significantly between 56.1 and 89.1% when compared with the original structures, which ranged between 57.1 and 67.3%. Fig. 4 presents the distribution of local temperatures over the mostly dilated [A] and mostly eroded [A_1] structures, as well as plots illustrating the effect of porosity [B] and specific surface [B_1] on the effective thermal conductivity of the combined "real" and "adapted" structures. Thermal conductivity was higher in the dilated materials than in the eroded structures, which can be attributed to the extremely low porosity in the formers [14,15,35]. Additionally, significant differences in the specific surfaces of both the "real" and the "adapted" structures were observed, as shown in Fig. 4B_1. The inverse and direct quadratic formulae, respectively, perfectly fit the trend of the effective thermal conductivity as it relates to material porosity and specific surface. Based on these plots, variation in pore size and specific surface has a minimal effect on foam-fluid systems' effective thermal conductivity, while the overlay of all plots in Fig. 4B shows that changes in the material porosity can significantly change the conductivity of porous media [18–21]. With pore sizes of 1 and 2 mm, and porosities of 76.76 and 76.33% respectively, the difference in their K_{eff} values usually amounts to 1.26%, despite the wide difference between their specific surfaces. Additionally, for porosities between 88.09 and 89.45%, with mean pore openings of 2 and 3 mm, significant differences in the effective thermal conductivity of the foam-fluid system were observed, which was 6.114 and 3.814W.m^{-1}. K^{-1} for the two cases. For samples characterized by mean pore size and porosity 1 mm and 88.27%, the effective thermal conductivity was estimated to be 7.127 W m^{-1} K^{-1}.

In practice, pore spaces may be filled with a variety of fluids, therefore the uncertainty of how cell size affects effective thermal conductivity is fundamental. Bhattacharya et al. [25] found that changing the cell size of metal foam had no effect on its thermal conductivity, while Paek et al. [17] reported that for constant porosity, decreasing effective thermal conductivity values were observed for decreasing cell size. Bovesecchi et al. [38] conducted numerical simulations that demonstrated the effective thermal conductivity of spherical cells can only be affected until a defined size is reached. Fig. 4 shows that significant changes in cell size have only a minimal impact on K_{eff} with constant porosity. The consistency in these changes is doubtful with K_{eff} slightly higher, in some cases, for smaller cell and K_{eff} scatter hard to discern from regression fits. Despite the importance of the topic within this field, research on the effects of bimodal arrangement (cells of different sizes) on K_{eff} for foam-fluid systems is lacking. In fact, several or all of the studies are focused on monomodal arrangements (monosized pores). A study in Ref. [31] demonstrated that the creation of bimodal structures is influenced by the addition of smaller (S–S) structures to larger (L-L) ones (Fig. 3), which leads to significant changes in pore connectivity, the size, porosity, surface area, and other properties of the porous matrix related to pore structures. The approach is used, therefore, to create 3D RVEs of bimodal arrangements and to vary the capillary radius from 10 to 80 μm, followed by advanced image creation

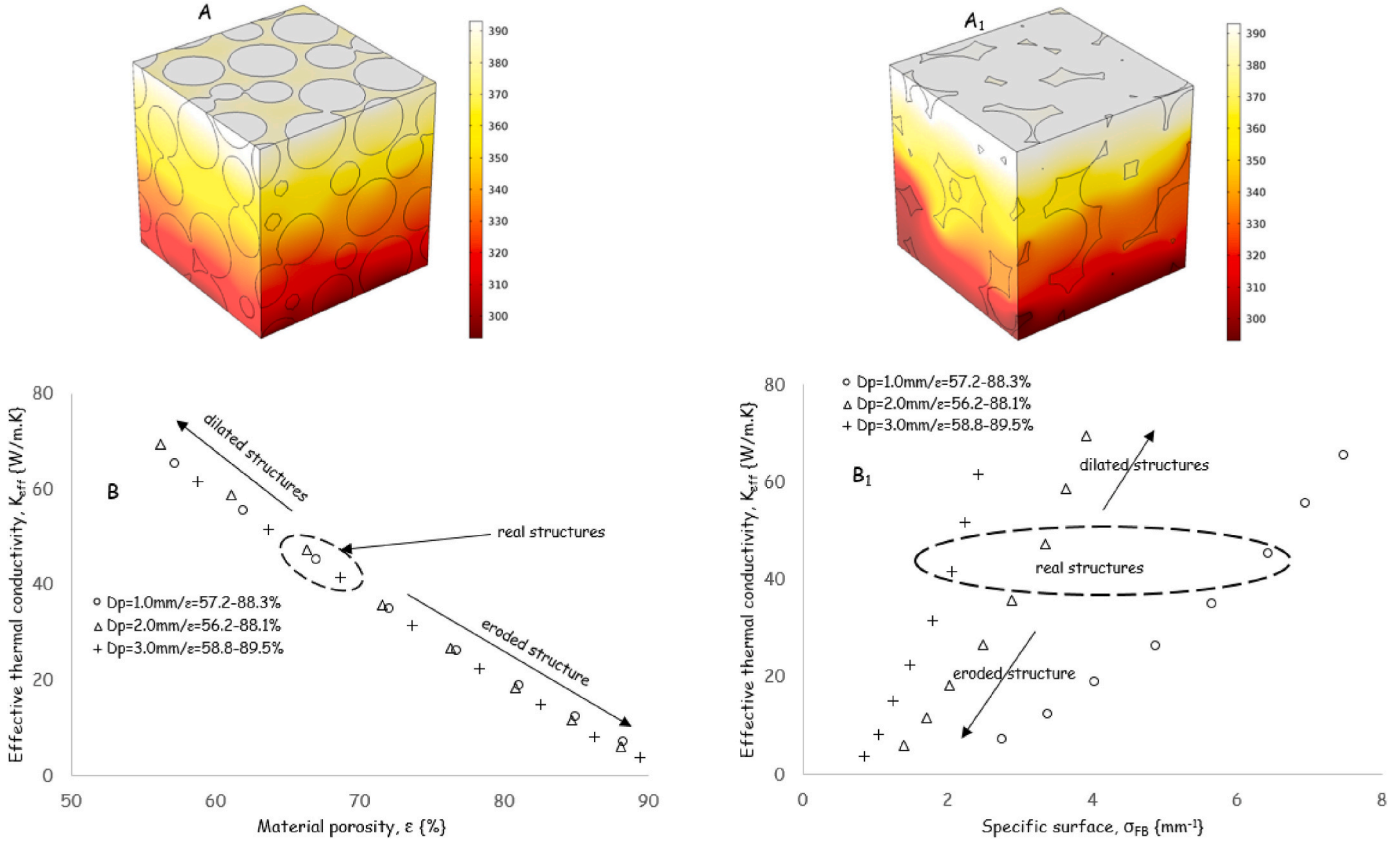

Fig. 4. The 3D RVE structurally-adapted virtual foam-fluid systems are shown at the top left [A] and right [A_1], showing typical temperatures {Kelvin} at the extremes of porosities, i.e. 55.156% and 88.089%, respectively. The bottom left [B] and right [B_1] represent plots of computed values of effective thermal conductivity against material porosity, ϵ {%} and specific surface, σ_{FB} {mm^{-1}}.

of the 3D RVEs and modelling of their effective thermal conductivity. Fig. 5 shows the morphology of the 3D RVEs of the structural phases (top) and distribution of temperature across air-filled monomodal (A_1 & A_4) and bimodal (A_2 & A_3) arrangements. Typically, the particle sizes of L-L and S–S monomodal structures are 2.0–2.5 mm and 0.5–1 mm, respectively. Approximately 12.5–50 vol per cent random packing is represented by bimodal structures with the addition of small spheres into larger ones.

Fig. 6 illustrates the marginal effects of adding smaller cells into larger cells (Fig. 6A) and material porosity (Fig. 6B) on the effective thermal conductivity of representative foam-fluid systems with varying capillary radius. Table 1 gives the pore-structure-related properties, effective thermal conductivity, and normalised K_{eff} of monomodal and bimodal cell structures. All the foam-fluid systems exhibit a constant decrease in effective thermal conductivity with increasing capillary radius, and the relationship between the effective thermal conductivity and additions (%) can be described as an inverse quadratic relationship (Fig. 6A). The effective thermal conductivity of the bimodal arrangements was noticeably low compared to the monomodal arrangements (Fig. 6B), due to significant changes in their porosities - higher for the bimodal arrangements and lower for the monosized pore structures. Table 1 shows that a continuous increase in the addition (%) of S–S in L-L structures increases their specific surfaces and ensures that their mean pore openings are consistently reduced, usually leading to a decrease in effective thermal conductivity. Additionally, Table 1 illustrates the effect of cell size on effective thermal conductivity for both monomodal and bimodal arrangements. For example, the average difference between the effective thermal conductivities of samples X_1, X_2 and X_3, with respective mean diameter sizes of 0.752, 2.320 and 2.04 mm and almost equal porosity (between 65.6% and 65.9%), ranges between 0.04 and 7.38%. Similarly, for samples Y_1 and Y_2 with porosities of 70.46 and 70.55%, respectively, the difference in effective thermal conductivity is calculated to be 5.97%. The numerical results indicate that substantial variations in specific surfaces are attributed to changes in cell size, and these differences contribute very little to their effective thermal conductivity, while changes in the material porosity of the macroporous structure significantly alter this thermofluidic property.

According to the data presented in both packing arrangements, the creation of bimodal structures perceptibly increases pore contact numbers and porosity, with the consequence that their effective thermal conductivity decreases. Observation of the 3D RVEs in Fig. 5 indicates that macroporous structures made by bimodal bead replication casting are expected to be more complex, as their effective thermal conductivity is expected to differ significantly from those structures with monosized pores. The capillary radius of both sphere-packing arrangements can be manipulated to achieve optimal and desirable heat transfer. In real replication casting, highly porous macroporous structures are produced at very low infiltration pressures (typically, below ¼ bar) and high packing density of beads (typically, above 70%). These materials can offer much wider pore openings, more pore contacts, and very high total porosities [1,33], thereby offering minimal resistance to flowing-dynamic fluids, reducing the effective thermal conductivity as shown in Fig. 6B. While such structures might be desirable for efficient fluid mixing, they have the downside of reduced load-bearing impact energy absorption compared to monomodal structures processed with much higher applied infiltration pressures (typically above 1 bar) and lower packing density (typically below 65%) [5,32].

So far, it has been demonstrated that changes in the pore-structure-related properties of cellular metallic components can significantly affect their overall effective thermal conductivity. Various experimental and predictive approaches reported in Refs. [15,23,28,39] have demonstrated that the estimation of K_{eff} can also be affected by the

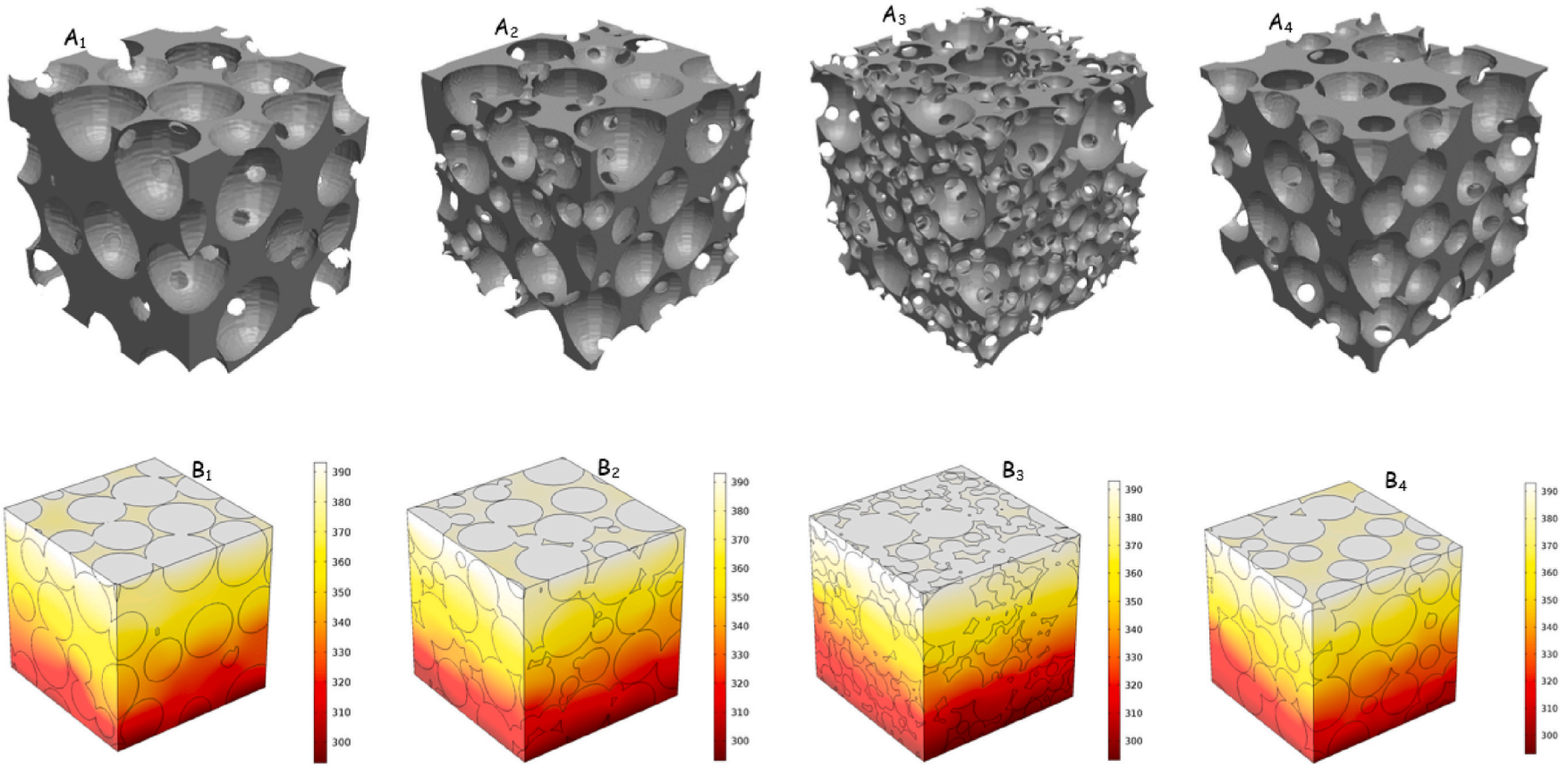

Fig. 5. Micro-geometrical representation of the 3D RVE structural phase (top) and temperature profile distribution (bottom) across the interstices of the foam–fluid systems for both monomodal (2.0–2.5mm/L-L ~ A_1 & B_1), (0.5–1.0mm/S–S ~ A_4 & B_4) and bimodal (12.5 vol% S–S ~ A_2 & B_2), (50 vol% S–S ~ A_3 & B_3) packing conditions.

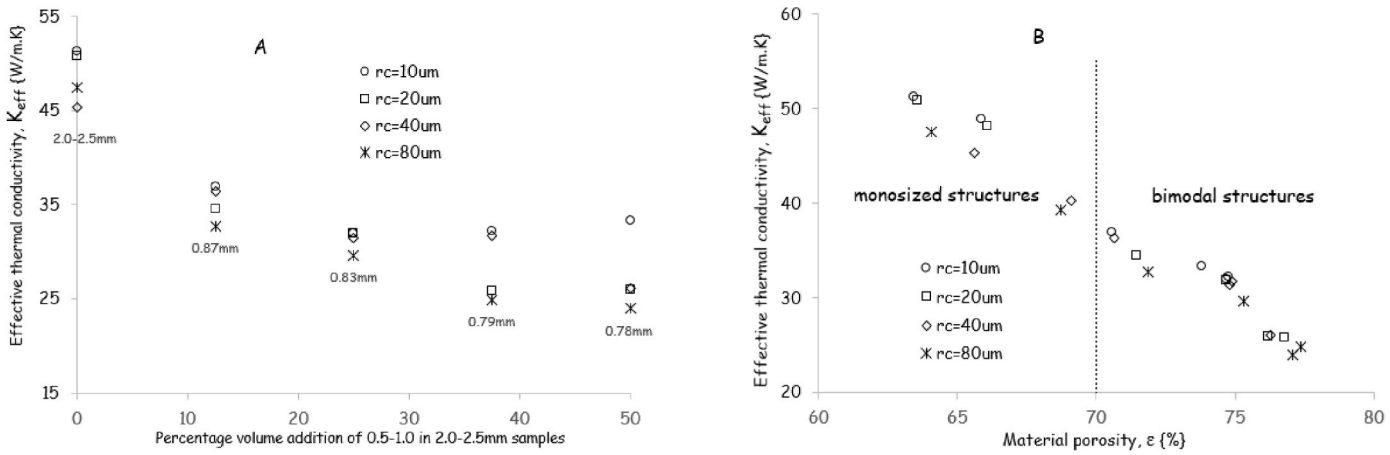

Fig. 6. Effective thermal conductivity plotted against percentage volume addition of S–S (0.5–1.0 mm) in L-L (2.0–2.5 mm) samples and against porosity of the materials.

Table 1
Pore-structure-related and conductive heat transfer properties for monomodal and bimodal virtual macroporous structures.

Particle size range D_s [mm]	Capillary radius, r_c [μm]	Mean pore diameter size size, D_p [mm]	Mean pore diameter opening, D_w [mm]	Foam porosity ϵ [%]	Specific surface, σ_{FB} [mm^{-1}]	Al-Air K_{eff} [W/m.K]	Al-Air K_{eff}/K_s [−]	Symbols
0.5–1.0 (S)	**10**	**0.752**	**0.149**	**65.884**	**7.983**	**48.941**	**0.206**	**X_1**
	20	0.753	0.195	66.071	7.805	48.162	0.202	
	40	0.773	0.249	69.093	7.019	40.305	0.169	
	80	0.818	0.304	68.719	6.728	39.347	0.165	
2.0–2.5 (L)	10	2.27	0.283	63.451	2.998	51.340	0.216	
	20	2.29	0.377	63.571	2.982	50.862	0.214	
	40	**2.32**	**0.499**	**65.629**	**2.782**	**45.345**	**0.191**	**X_2**
	80	2.36	0.647	64.044	2.751	47.519	0.200	
12.5 vol%S	20	0.866	0.263	71.435	3.191	34.518	0.145	
25.0Vo%S		0.831	0.235	74.698	3.703	31.933	0.134	
37.5 vol%S		0.792	0.221	76.798	3.573	25.888	0.109	
50.0 vol%S		0.779	0.212	76.198	4.038	25.973	0.109	
2.04	**10**	**2.040**	**0.271**	**65.959**	**3.296**	**48.831**	**0.205**	**X_3**
1.02	**80**	**1.040**	**0.375**	**70.458**	**5.052**	**34.770**	**0.146**	**Y_1**
12.5 vol%S	**10**	**0.866**	**0.262**	**70.554**	**3.385**	**36.979**	**0.155**	**Y_2**

solid/fluid properties. Although most K_{eff} studies on cellular metallic structures involve alumina-air, matrices saturating with water and other base metals are rare. Therefore, the steady-state computed conductive heat transfer for all foam-fluid systems was resolved, changing both the fluid and solid properties. Fig. 7A plots computed values of K_{eff} against total material porosity considering air and water as saturating fluids whilst pure aluminium (Al), aluminium alloy (Al3003–H18), alumina and concrete as base solids. Aluminium foam appears to transfer heat by far the most, as it has the highest computed heat flux of all the base metals. The reason for this may be attributed to its extremely high thermal conductivity which is over 100 times higher than that of concrete foam and 35% higher than Al3003–H18 and more than 8x higher than alumina foams. Additionally, the highest improvement in the value of K_{eff} occurred for the Al-Water system; a few percentage points higher than for the Al-Air system, which supports previous studies [11,21,36] on the critical role of fluids-in-pores on overall heat transfer phenomena. As an example, at the extremities of total material porosities (usually between 56.16 and 89.45%), the water-in-pore influence changes gradually from 0.9 to 37.4% compared to air-saturated aluminium porous structures. Similarly, the creation of bimodal structures increases the volume fraction of material pores from 0.63 to 0.76 (20% increment) while reducing the effective thermal conductivity only from 1.40 to 3.39%. Thus, based on these observations and the following plots in Fig. 7B and C, it is reasonable to conclude that the effective thermal conductivity of cellular metallic components increases as the value of the solid-fluid conductivity ratio (K_S/K_f) increases [19–21]. Fig. 7D also provides plots of the numerically simulated results of the normalised K_{eff} of the Al-Air system with experimental measurements taken from the literature. The computed values of normalised effective thermal conductivity agree with the experimental scatter provided in Refs. [28,29]. In part, this phenomenon can be explained by the similarity in porosity ranges considered here, which typically range between 55 and 90%. While computed values for K_{eff} closely match experimental measurements in Ref. [28], slight differences between numerical modelling and experimental measurements in Ref. [29] could be attributed to structural defects arising from non-uniformity of the foam matrices.

Aside from macroporous/cellular structure, solid content also impacts the effective thermal conductivity of granular materials, such as fly ash [40] and binary soil [41]. However, the effective thermal conductivity of these materials differs greatly from that of cellular structures, a result that can be explained by the strong dependence of gas thermal conductivity on the confined gas pressure within the interstices of the packed granular materials [42]. Compared to the geometrical dimension of the confined space (cells) in cellular materials, the mean free path is so small that the pressure drop is higher, the Knudsen effect is negligible, and the thermal conductivity of the gas is independent of pressure. In packed structures, gas molecules interact more sporadically, and the heat is predominantly transferred by interactions between the gas molecules and the walls [42]. This results in the gas thermal conductivity becoming strongly dependent on the gas pressure. Accordingly, modelling predictions of heat transfer in packed structures differ significantly from predictions of heat transfer in cellular materials. In

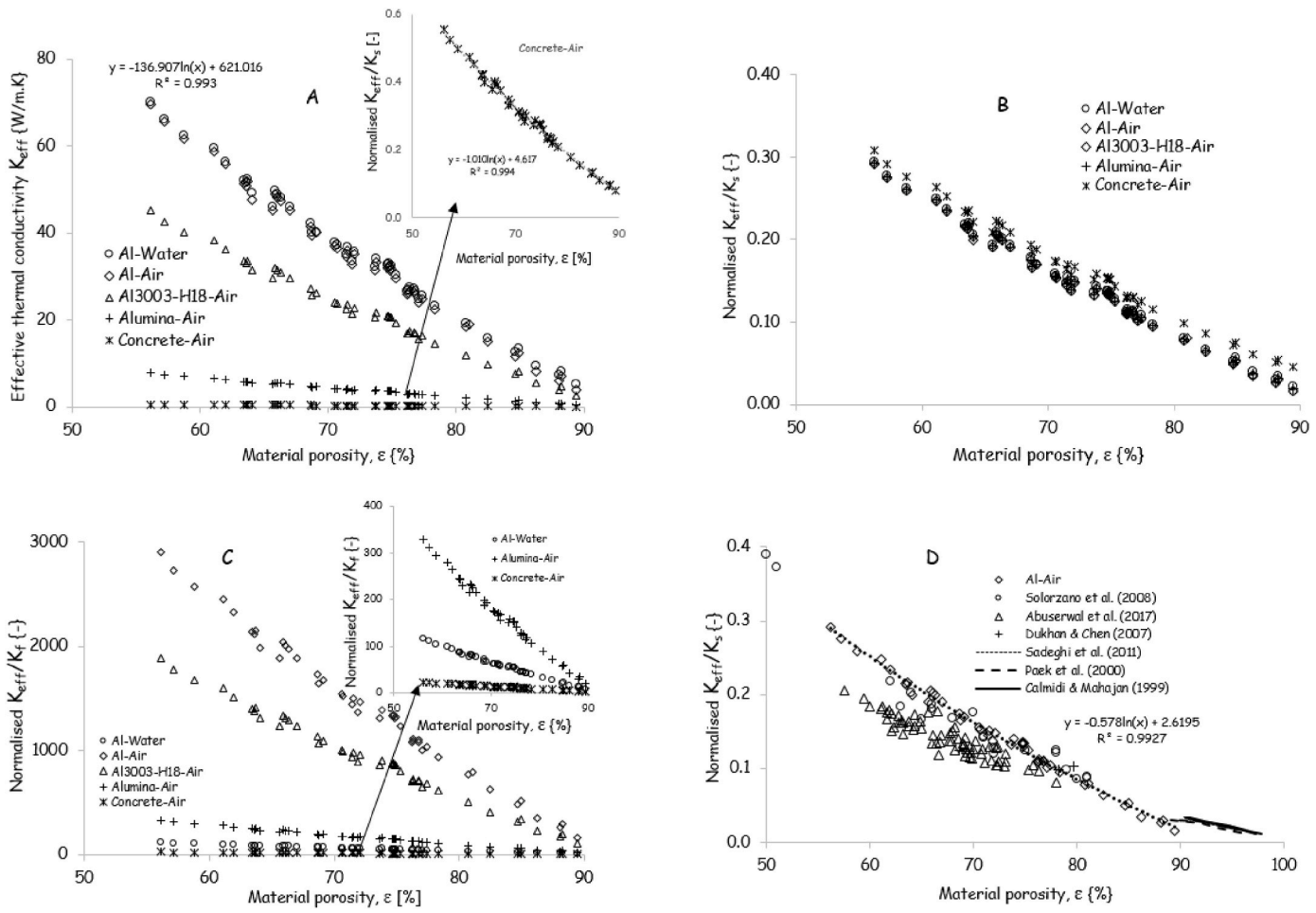

Fig. 7. Plots of effective thermal conductivity, K_{eff} {W.m^{-1}. K^{-1}} [A] and normalised effective thermal conductivity (solid-phase), K_{eff}/K_s {-} [B] against material porosity, ϵ {%} for all samples showing effect imposed by material and fluid properties. Fig. 7C is the normalised effective thermal conductivity (fluid-phase), K_{eff}/K_f {-} against material porosity, ϵ {%} while Fig. 7D is computed and experimental measurements of normalised effective thermal conductivity (solid-phase), K_{eff}/K_f {-} against material porosity ϵ {%}.

addition to the pore-level numerical models so far described, pre-existing literature [15,19,43–45] offers numerous examples of the mathematical relationship between foam-fluid thermal conductivity and porosity, fluid thermal conductivity, and solid thermal conductivity. Several of these models were based on cellular structures and sponges with high porosity, typically exceeding 90%. In some cases, they used empirical constants to account for manufacturing variability and operating conditions when describing the effective thermal conductivities of these complex microstructures. Fig. 7 shows that the structures considered herein have lower porosities; even with bimodal matrices and adapted matrices, their porosities are still lower than "tetrakaidecahedron-type" structures, as reported in the literature [19–24]. As a result, predictions using available mathematical correlations of effective thermal conductivity of high porosity foams are not necessarily expected to overlay computationally computed data and experimental measurements [28,29] for low porosity foams. Furthermore, empirical relationships for low porosity foams in Ref. [29] described the dependence of effective thermal conductivity on porosity but neglected the role of capillary radius. It is, therefore, desirable to define an expression that predicts the effective thermal conductivity of porous metallic components taking into account other pore-structure characteristics. For what the computed data concerns, a mathematical inference that shows the dependence of effective thermal conductivity (K_{eff}) on specific surface (σ_{FB}, [m^{-1}]), mean pore diameter opening (D_w), total material porosity (ϵ) and thermal conductivity of the solid matrix (k_s) can be expressed as follows:

$$\frac{K_{eff}}{K_s} \propto \frac{\sigma_{FB}^{m_1}}{D_w^{m_2}}[1-\varepsilon]^{m_3} \quad 3$$

where m_1, m_2& m_3 are empirical parameters which can be determined using the least mean square method (LSM). Eqn (3) can be re-written as:

$$\frac{K_{eff}}{K_s} = \beta \frac{\sigma_{FB}^{m_1}}{D_w^{m_2}}[1-\varepsilon]^{m_3} \quad 4$$

where β is an empirical constant.

By taking the logarithm of both sides of Eqn (4) we get the following expression:

$$\ln\left(\frac{K_{eff}}{K_s}\right) = ln\beta + m_1 ln\sigma_{FB} - m_2 \ln D_w + m_3 \ln(1-\varepsilon) \quad 5$$

Multiple linear regression of $\ln\left(\frac{K_{eff}}{K_s}\right)$ against $ln\sigma_{FB}$, $\ln D_w$ and can be performed to determine the best estimate of the unknown $ln\beta$, m_1, m_2 *and* m_3. The values obtained are −0.6110, 0.093, 0.0114, 1.7171. From the datum β results 0.5428. In the case of the ratio between effective thermal conductivity (K_{eff}) and fluid thermal conductivity (K_f), values for $m_o(ln\beta), m_1$, m_2 & m_3 equal to 9.5583, 0.0405, −0.0347 and 1.8850 and a constant β as 14,161.75 were obtained. Following are two mathematical expressions considering the effect of pore-structures on effective thermal conductivity, solid (Eqn (6)) and fluid (Eqn (7)) thermal conductivity.

$$\frac{K_{eff}}{K_s} = 0.5428 \frac{\sigma_{FB}^{0.093}}{D_w^{0.0114}} (1-\epsilon)^{1.7171} \quad 6$$

$$\frac{K_{eff}}{K_f} = 14161.75 \frac{\sigma_{FB}^{0.0405}}{D_w^{-0.0347}} (1-\epsilon)^{1.8450} \quad 7$$

Fig. 8 plots predicted data from equations (6) and (7), using the empirical models in Refs. [15,22,25,26,28,29,46] and experimental measurements in Ref. [28] of the normalised effective thermal conductivity versus the total material porosity [%]. On these plots, it is evident that the results obtained using equations (6) and (7) are entirely consistent with experimental measurements in Ref. [28] but slightly different from predictions using models developed in Ref. [29]. Possibly, this has to do with nonhomogeneity in the cellular walls of porous matrices as well as structural defects and changes in the surface area of the materials. Conversely, predictions in Refs. [15,22,25,26,46] exhibited a linear inverse relationship between thermal conductivity and porosity but considerably deviated from predictions based on equations (6) and (7). This correlates with our earlier observation that models developed for high porosity foams such as those developed in Refs. [15,22,25,26,45] may not be suitable for predicting the behaviour of low-porosity foams. An inverse non-linear relationship was found to be more fitting for the trend of effective thermal conductivity in low-porosity foams, which decreases as the porosity increases. Comparing the results to predictions derived from models of high porosity foams, effective thermal conductivity was observed to be higher for the majority of porosity values, typically below 80%. In addition, Fig. 8 illustrates that, beyond 80% porosity, numerical predictions and values obtained using equations (6) and (7) were significantly lower than predictions and experiments for high porosity foams. This is a contrast to earlier observations and may be attributed to continuous erosion on the material surfaces. Structures with eroded surfaces were created by modifying the "real" or "original" virtual structures (created from the sphere packing models) into more porous structures. This was achieved by simply subtracting pixel elements (25 μm voxel size) from the solid field, which is equivalent to applying lower differential pressure during casting of porous metallic structures [1,6,33]. In turn, this resulted in the macroporous structures becoming more porous, with wider pore openings and a reduction in the solid content (available for heat transfer). With more than four pixels removed, some of the material's features are lost, resulting in a significant reduction of the strut thickness and surface area of the base structure, which has been shown to be responsible for conductive heat transfer. As a result of erosion, the pore volume available for efficient fluid mixing and transfer can increase, but at the expense of reduced thermal conductivity of the foam-fluid system. Hence, this approach might be useful in gaining a better understanding of the effects of changes in macroporous structures on conductive heat transport phenomena, without needing to produce test samples.

It is noteworthy that geometrical descriptions of the cellular structures considered herein are hardly identifiable as bottleneck-like structures, which are characteristic of near-circular pore connections and pore walls. Based on previous observations, it is not surprising that analytical and empirical models for high-porosity foams (most commonly known as the Kelvin "tetrakaidecahedron") do not adequately capture the behaviour at the boundary layer at the scale of the near-circular pores (where a transition in relaxation behaviour occurs [47,48]) exhibited by the low-porosity "bottleneck-type" foams. Porous materials with a low porosity tend to have higher surface areas (specific surfaces) than higher porosity materials [7,35,49], so they have higher values for effective thermal conductivity. Fig. 7D shows a comparison between the effective thermal conductivities of "bottleneck" and "tetrakaidecadron" porous matrices but does not fully include the contributions of the capillary radius and specific surfaces. Additionally, the linear inverse calculations for effective thermal conductivity against porosity (normally below 80%) plotted in Fig. 8 using models for high porosity foams do not necessarily hold true when tested against experimental measurements and simulations for similar porosity and pore morphology of similar material types. It is, therefore, strongly recommended to adopt the dilation approach used here to create low-porosity semi-virtual structures of the "tetrakaidecahedron-type" and apply simulations to assess the conductive heat transfer between the "real" and "simulation" matrices. This approach, coupled with experimental measurements of conductive heat transfer for low-porosity foams, may allow for differentiation of the impact of the morphology of the pore morphology of the bottleneck and tetrakaidecahedron structures on their effective thermal conductivity.

4. Conclusion

A pore-level computational fluid dynamics modelling and simulation of the effective thermal conductivity of macroporous structures using sphere-packing was found to be an excellent fit to experimental measurements of metal foams with "bottleneck-type" structures but deviated significantly from both experimental measurements and models for high porosity foams. Based on sphere-packing models, bimodal structures and adapted structures were developed which take into account porosity, pore openings (or capillary action) and surface specificity on the effective thermal conductivity of these low-porosity structures. With an increase in capillary radius from 10 to 80 μm in sphere packing

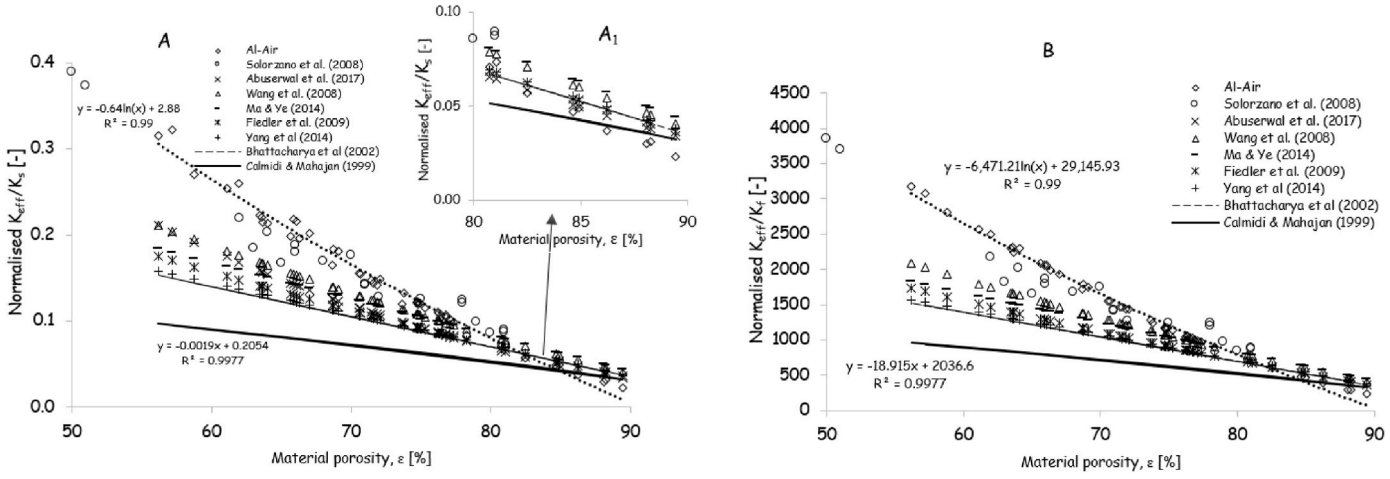

Fig. 8. Plots of normalised effective thermal conductivity against material porosity, ϵ {%} for the solid-phase, K_{eff}/K_s [A] and fluid-phase, K_{eff}/K_f [B], using the empirically derived model and several other models available in the literature.

models, porosity increases from 0.63 to 0.70 and bimodal and eroded structures increase the fluid's ability to traverse the material. These factors have likely increased the original monomodal fluid volume by 17 and 30%, respectively. The numerical simulations for these structures also revealed that variations in the solid-fluid conductivity ratio with varying material porosity may lead to changes in the effective thermal conductivity of cellular foams. An increase in the conductivity ratio was found to increase the effective thermal conductivity of the foam-fluid systems - with aluminium-water and concrete-air systems respectively showing the highest and lowest contributions to the heat transport phenomena. The sphere-packing modelling method proved to be a valuable tool for optimizing the thermal performance of a class of porous structures offering further fluid-dynamical and mechanical advantages, such as fluid mixing and load-bearing capability.

Credit's author statement

Otaru, A.J: Software, Conceptualization, Methodology, Software, Writing-Original draft preparation, Supervision, **Isa, R.O., Emene A.U.:** Data curation, Visualization, Investigation, Validation, Formal analysis, Resources. & **Faruq, A.A:** Data curation, Visualization, Investigation, Validation, Formal analysis, Resources, **Sedemogun, P.O:** Writing-Reviewing and Editing, Project administration, Formal analysis. &; **Hassan, S.M.:** Writing-Reviewing and Editing, Project administration, Formal analysis.

Declaration of competing interest

The authors declare that they have no known competing financial interests or personal relationships that could have appeared to influence the work reported in this paper.

Acknowledgement

Dr. AJ would like to thank the University of Nottingham – United Kingdom, Federal University of Technology Minna – Nigeria, Petroleum Technology Development Fund – Nigeria, Bowers and Wilson Group - United Kingdom, Simpleware-Synopsys Limited – United States of America for their financial assistance, technical support and licenses needed for the successful completion of this work. Special thanks to Prof. Andrew R. Kennedy (University of Lancaster – United Kingdom) for whom I have learnt a lot and for his enormous contributions to the synthesis and applications of porous metallic components.

References

[1] A.J. Otaru, H.P. Morvan, A.R. Kennedy, Airflow Measurement across Negatively-Infiltration Processed Porous Aluminium Structures, vol. 65, American Institute of Chemical Engineers AIChE J, 2019, pp. 1355–1364.
[2] P.A. Jorges, J.C. Malcom, Recent-trends in porous sound-absorbing materials, Sound Vib. 44 (2010) 12–17.
[3] A.J. Otaru, M.B. Samuel, Pore-level CFD investigation of velocity and pressure dispositions in microcellular structures, M.B. Mater. Res. Express 8 (2021), 046516
[4] L.-P. Lefebvre, J. Banhart, D.C. Dunand, Porous metals and metallic foams: current status and recent developments, Adv. Eng. Mater. 10 (9) (2008) 775–787.
[5] P. Asholt, J. Ashby Banhart, F. M, N.A. Fleck, in: Bremen (Ed.), Metal Foams and Porous Metal Structures, MIT-Verlag, Germany, 1999, p. 133.
[6] A.R. Kennedy, Porous metals and metal foams made from powders, Powder Metall. (2012), https://doi.org/10.5772/33060.
[7] M.F. Ashby, L.U. Tianjin, Metal foams: a survey, Sci. China, Ser. A 46 (6) (2003) 521–530.
[8] A.J. Otaru, H.P. Morvan, A.R. Kennedy, Modelling and optimisation of sound absorption in replicated microcellular metals, Scripta Mater. 150 (2018) 152–155.
[9] P. Langston, A.R. Kennedy, Discrete element modelling of the packing of spheres and its application to the structure of porous metals made by infiltration of packed beds of NaCl beads, Powder Technol. 268 (2014) 210–218.
[10] S.E. Susilowati, A. Fudholi, D. Sumardiyanto, Mechanical and Microstructural characteristics of Cu–Sn–Zn/Gr metal matrix composites processed by powder Metallurgy for bearing materials, Result. Eng. 22 (2022) 100377.
[11] P. Ranut, E. Nobile, L. Mancini, High-resolution Microtomography-based CFD simulation of flow and heat transfer in aluminium metal foams, Appl. Therm. Eng. 69 (1–2) (2013) 230–240.
[12] G. Walther, U. Gaitzsch, T. Buttner, B. Kieback, T. Weibgarber, R. Kolvenbach, M. Lincke, Application of metal foam as catalyst carrier, in: Euro PM2017 – Foams, 2017.
[13] B. Ozmat, B. Leyda, B. Benson, Thermal applications of open-cell metal foams, Mater. Manuf. Proc. 19 (5) (2004) 839–862.
[14] P. Ranut, E. Nobile, On the effective thermal conductivity of metal foams, J. Phys. Conf. 547 (2014), 012021.
[15] V.V. Calmidi, R.L. Mahajan, The effective thermal conductivity of high porosity fibrous metal foams, ASME J. Heat Trans. 121 (1999) 466–471.
[16] R. Dyga, S. Witczak, Investigation of effective thermal conductivity of aluminium foams, Procedia Eng. 42 (2012) 1088–1099.
[17] J.W. Paek, B.H. Kang, S.Y. Kim, J.M. Hyun, Effective thermal conductivity and permeability of aluminium foam materials, Int. J. Thermophys. 21 (2) (2000) 453–464.
[18] K. Boomsma, D. Poulikakos, On the effective thermal conductivity of a three-dimensional structured fluid-saturated metal foam, Int. J. Heat Mass Tran. 44 (2001) 827–836.
[19] Z. Dai, K. Nawaz, Y.G. Park, J. Bock, A.M. Jacobi, Correcting and extending the Boomsma–Poulikakos effective thermal conductivity model for three-dimensional, fluid-saturated metal foams, Int. Commun. Heat Mass Tran. 37 (2010) 575–580.
[20] K. Boomsma, D. Poulikakos, Corrigendum for the paper: K. Boomsma, D. Poulikakos, "On the effective thermal conductivity of a three-dimensionally structured fluid-saturated metal foam" [International Journal of Heat and Mass Transfer, 44, 2001, Int. J. Heat Mass Tran. 54 (2011) 827–836, 746-748..
[21] X. Fan, X. Ou, F. Xing, G.A. Turley, P. Denissenko, M.A. Williams, N. Betail, C. Pham, A.A. Lapkin, Microtomography-based numerical simulations of heat transfer and fluid flow through $\beta - SiC$ open-cell foams for catalysis, Catal. Today 278 (2) (2016) 350–360.
[22] M. Ma, H. Ye, An image analysis method to obtain the effective thermal conductivity conductivity of metallic foams via a reduced concept of shape factor, Appl. Therm. Eng. 73 (2014) 1279–1284.
[23] X.H. Yang, J.J. Kuang, T.J. Lu, F.S. Han, T. Kim, A simplistic analytical Unit cell based model for the effective thermal conductivity of high porosity open-cell metal foams, J. Phys. D 46 (2013), 255302.
[24] H. Yang, J.X. Bai, Y.B. Yan, J.J. Kuang, T.J. Lu, T. Kim, An analytical Unit cell model for the effective thermal conductivity of high porosity open-cell metal foams, Transport Porous Media 102 (2014) 403–426.
[25] A. Bhattacharya, V.V. Calmidi, R.L. Mahajan, Thermophysical properties of high porosity metal foams, Int. J. Heat Mass Tran. 45 (2002) 1017–1031.
[26] T. Fiedler, E. Solorzano, A. Garcia-Moreno, F. Ochsner, I. Belova, G. Murch, Lattice Monte Carlo and experimental analyses of the thermal conductivity of random-shaped cellular aluminium, Adv. Eng. Mater. 11 (10) (2009) 843–847.
[27] N. Dukhan, K.-C. Chen, Heat transfer measurements in metal foam subjected to constant heat flux, Exp. Therm. Fluid Sci. 32 (2007) 624–631.
[28] E. Solorzano, J.A. Reglero, M.A. Rodriguez-Perez, D. Lehmbus, M. Wichman, J. A. de Saja, An experimental study on the thermal conductivity of aluminium foams by using the transient plane source method, Int. J. Heat Mass Tran. 51 (2008) 6259–6267.
[29] A.F. Abuserwal, E.M.E. Luna, R. Goodall, R. Woolley, The effective thermal conductivity of open cell replicated aluminium metal sponges, Int. J. Heat Mass Tran. 108 (B) (2017) 1439–1448.
[30] J. Skibinski, K. Cwieka, S.H. Ibrahim, T. Wejrzanowski, Influence of pore size variation on thermal conductivity of open-porous foams, Materials 12 (2019) 1–10.
[31] P. Langston, A.R. Kennedy, Discrete element modelling of the packing of spheres and its application to the structure of porous metals made by infiltration of packed beds of NaCl beads, Powder Technol. 268 (2014) 210–218.
[32] A.J. Otaru, A.R. Kennedy, The permeability of virtual macroporous structures generated by sphere packing models: comparison with analytical models, Scripta Mater. 124 (2016) 30–33.
[33] A.J. Otaru, H.P. Morvan, A.R. Kennedy, Measurement and simulation of pressure drop across replicated microcellular aluminium in the Darcy-Forchheimer Regime, Acta Mater. 149 (2018) 265–275.
[34] S. Krishnan, J.Y. Murthy, S.V. Garimella, Direct simulation of transport in open-cell metal foam, ASME J. Heat Trans. 128 (2006) 793–799.
[35] M.S. Phanikumar, R.L. Mahajan, Non-Darcy natural convection in high porosity metal foams, Int. J. Heat Mass Tran. 45 (2002) 3781–3793.
[36] X. Xiao, P. Zhang, M. Li, Effective thermal conductivity of open-cell metal foams Impregnated with pure paraffin for latent heat storage, Int. J. Therm. Sci. 81 (2014) 94–105.
[37] A. Tessarin, M. Zaccariotto, U. Galvanetto, D. Stocchi, A Multiscale numerical Homogenization-based method for the prediction of Elastic properties of components produced with the Fused deposition modelling process, Result. Eng. 14 (2022) 100409.
[38] G. Bovesecchi, P. Coppa, M. Potenza, A numerical model to Explain experimental results of effective thermal conductivity measurements on Unsaturated soils, Int. J. Thermophys. 38 (2017) 1–14, https://doi.org/10.1007/s10765-017-2202-1. ISSN: 0195-928X.
[39] E. Schmierer, A. Razani, Thermal boundary to open-celled metal foams contact conductance, Mater. Sci. (2006), https://doi.org/10.2514/6.2006-3398.
[40] X. Kang, L. Ge, Enhanced series-parallel model for estimating the time-dependent thermal conductivity of fly ash soil Mixtures, Granul. Matter 17 (5) (2015) 579–592, https://doi.org/10.1007/s10035-015-0577-x.
[41] Z. Xia, R. Chen, X. Kang, Laboratory characterization and modelling of the thermal-mechanical properties of binary soil Mixtures, Soils Found. 59 (2019) 2167–2179.

[42] M. Moscardini, Y. Gan, S. Pupeshi, M. Kamlah, Discrete element method for effective thermal conductivity of packed pebbles accounting for smoluchowski effect, Fusion Eng. Des. 127 (2018) 192–201.
[43] R. Singh, H. Kasana, Computational aspects of effective thermal conductivity of high porosity metal foams, Appl. Therm. Eng. 24 (2004) 1841–1849.
[44] R. Singh, S. Kumar, R. Beniwal, Bounding of effective thermal conductivity of two-phase materials, Defect Diffusion Forum 336 (2013) 185–193.
[45] S. Ackermann, J. Scheffe, J. Duss, A. Steinfeld, Morphological characterization and effective thermal conductivity of dual-scale Reticulated porous structures, Materials 7 (2014) 7173–7195.
[46] J. Wang, J. Carson, J. Willix, M. North, D. Cleland, A symmetric and interconnected skeleton structures (SISS) model for predicting thermal and Electrical conductivity and young's modulus of porous foams, Acta Mater. 56 (2008) 5138–5146.
[47] D.K. Wilson, Relaxation-matched modelling of propagation through porous media, including fractal structures, J. Acoust. Soc. Am. 94 (2) (1993) 1136–1145.
[48] A.J. Otaru, Z. Manko, O.E. Odumu, A.G. Isah, M.R. Corfield, Numerical Modelling and Optimisation of Reverberation Cutback for Packed Spheres, Journal of King Saud University – Engineering Sciences, 2021, https://doi.org/10.1016/j.jksues.2021.08.005.
[49] A.J. Otaru, M. Abdulkadir, A.S. Kovo, M.R. Corfield, N. Tanko, O.A. Odey, A. Kenfack, U.O. Aroke, Three-dimensional high-resolution image inversion and pore level CFD characterization of effective thermal conductivity of replicated microcellular structures, Int. J. Thermofluids 14 (2022), 100141.